Experimentally-constrained biophysical models of tonic and burst firing modes in thalamocortical neurons

Elisabetta Iavarone[1*], Jane Yi[2], Ying Shi[1,2], Bas-Jan Zandt[1], Christian O'Reilly[1], Werner Van Geit[1], Christian A. Rössert[1], Henry Markram[1,2], and Sean L. Hill[1,3]

[1]Blue Brain Project, École polytechnique fédérale de Lausanne (EPFL), Geneva, Switzerland

[2]Laboratory of Neural Microcircuitry (LNMC), École polytechnique fédérale de Lausanne (EPFL) (EPFL), Lausanne, Switzerland

[3]Krembil Centre for Neuroinformatics, CAMH, Toronto, Canada

* Corresponding author

E-mail: elisabetta.iavarone@epfl.ch

Abstract

Somatosensory thalamocortical (TC) neurons from the ventrobasal (VB) thalamus are central components in the flow of sensory information between the periphery and the cerebral cortex, and participate in the dynamic regulation of thalamocortical states including wakefulness and sleep. This property is reflected at the cellular level by the ability to generate action potentials in two distinct firing modes, called tonic firing and low-threshold bursting. Although the general properties of TC neurons are known, we still lack a detailed characterization of their morphological and electrical properties in the VB thalamus. The aim of this study was to build biophysically-detailed models of VB TC neurons explicitly constrained with experimental data from rats. We recorded the electrical activity of VB neurons (N = 49) and reconstructed morphologies in 3D (N = 50) by applying standardized protocols. After identifying distinct electrical types, we used a multi-objective optimization to fit single neuron electrical models (e-models), which yielded multiple solutions consistent with the experimental data. The models were tested for generalization using electrical stimuli and neuron morphologies not used during fitting. A local sensitivity analysis revealed that the e-models are robust to small parameter changes and that all the parameters were constrained by one or more features. The e-models, when tested in combination with different morphologies, showed that the electrical behavior is substantially preserved when changing dendritic structure and that the e-models were not overfit to a specific morphology. The models and their analysis show that automatic parameter search can be applied to capture complex firing behavior, such as co-existence of tonic firing and

low-threshold bursting over a wide range of parameter sets and in combination with different neuron morphologies.

Author summary

Thalamocortical neurons are one of the main components of the thalamocortical system, which are implicated in key functions including sensory transmission and the transition between brain states. These functions are reflected at the cellular level by the ability to generate action potentials in two distinct modes, called burst and tonic firing. Biophysically-detailed computational modeling of these cells can provide a tool to understand the role of these neurons within thalamocortical circuitry. We started by collecting single cell experimental data by applying standardized experimental procedures in brain slices of the rat. Prior work has demonstrated that biological constraints can be integrated using multi-objective optimization to build biologically realistic models of neuron. Here, we employ similar techniques as those previously employed, but extend them to capture the multiple firing modes of thalamic neurons. We compared the model results with additional experimental data test their generalization and quantitatively reject those that deviated significantly from the experimental variability. These models can be readily integrated in a data-driven pipeline to reconstruct and simulate circuit activity in the thalamocortical system.

56 ## Introduction

57 Thalamocortical (TC) neurons are one of the main components of the thalamus and have
58 been extensively studied *in vitro* and *in computo*, especially in first order thalamic nuclei in
59 different species (1). One of these nuclei, namely the ventral posterolateral nucleus (VPL), relays
60 somatosensory, proprioceptive, and nociceptive information from the whole body to the
61 somatosensory (non-barrel) cortex (2). The VPL is located close to ventral posteromedial nucleus
62 (VPM), which transmits information from the face to the barrel cortex. The VPL and VPM nuclei
63 constitute the ventrobasal (VB) complex of the thalamus (3).

64 Despite its key role in sensory functions, a systematic characterization of the cellular
65 properties of the VB complex is still missing. The morphologies of VPL neurons in adult rats were
66 described in early anatomical studies but were limited to two-dimensional drawings of Golgi-
67 impregnated cells (4). The general electrical properties of TC neurons maintained *in vitro* are
68 known and similar in different thalamic nuclei and species with respect to the generation of two
69 distinct firing modes, called tonic firing and low-threshold bursting (5–8). However, a systematic
70 description on the electrical types in the VB thalamus in the rodents is still missing.

71 Collecting morphological and electrophysiological data, by following standardized
72 experimental procedures, is essential for the definition of cells types and it is the first step to
73 constraining computational models of single neurons (9,10). Although models of TC neurons have
74 already been previously published, they typically were aimed at studying specific firing properties
75 and their parameters were hand tuned to achieve the desired result (11–15).

76 The purpose of our study is to systematically define the morphological and electrical types
77 by collecting *in vitro* experimental data and to constrain biophysically detailed models of VB TC

78 neurons of the juvenile rat. To the best of our knowledge, automatic parameter search has not
79 been applied, thus far, to capture complex firing behavior in thalamic neurons, in particular low-
80 threshold bursting and tonic firing. We defined the electrical and morphological types of TC
81 neurons through in vitro patch-clamp recordings and 3D morphological reconstructions. We then
82 extended an existing method (16) to account for their distinctive firing properties. These
83 electrical models (e-models) were constrained by the electrical features extracted from
84 experimental data (9,17,18). Other experimental data were used to assess the generalization of
85 the models to different stimuli and morphologies. We further performed a sensitivity analysis by
86 varying each parameter at a time by a small amount and recording the resulting electrical
87 features. This analysis provides an assessment of the robustness of the models and a verification
88 that the selected features provide sufficient constraints for the parameters.

89 ## Results

90 ### Physiological and morphological characterization

91 We characterized TC neurons in slices of the rat VB thalamus, by combining whole-cell patch-
92 clamp recordings, biocytin filling and 3D Neurolucida (MicroBrightField) reconstruction, along
93 with anatomical localization in a reference atlas (19) (Fig 1).
94

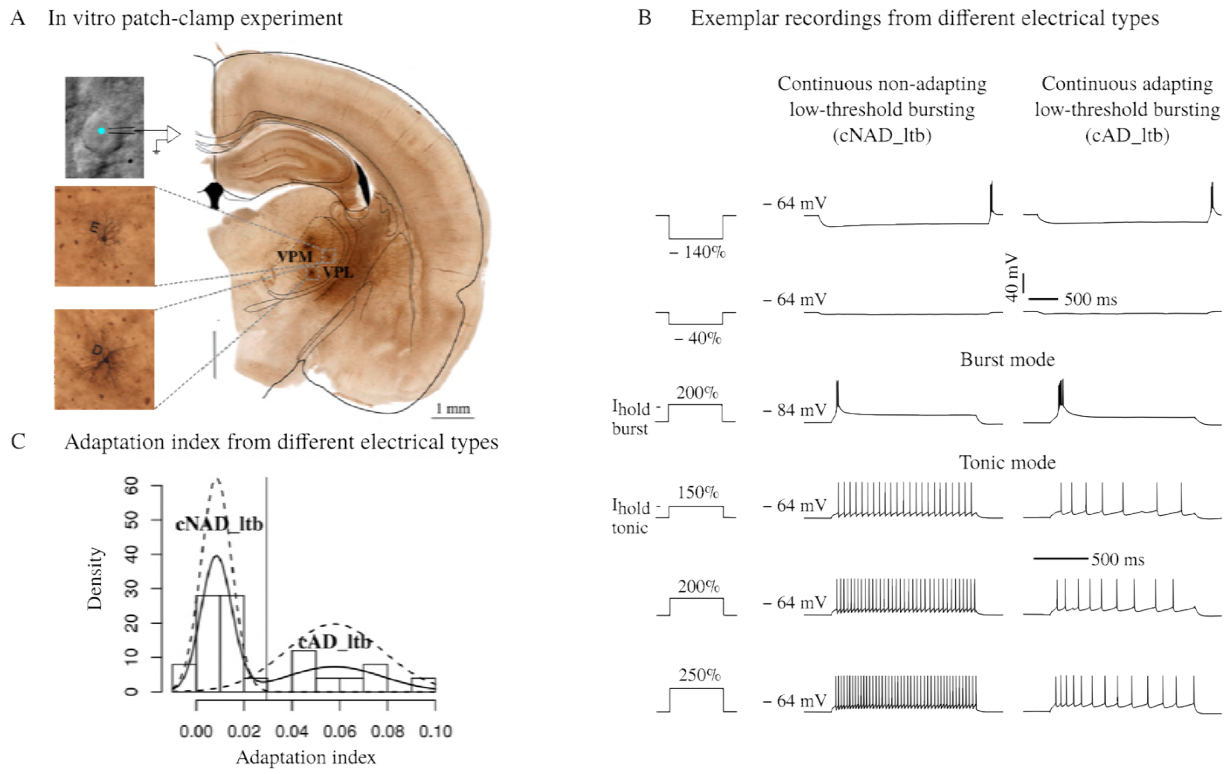

Figure 1: Simultaneous physiological and morphological characterization.

(A) View of a patched cell under optic microscope and anatomical localization of biocytin-filled neurons (insets) in the rat Paxinos and Watson atlas (19). Letters D and E identify morphologies in a slice. (B) Voltage responses of two different thalamocortical (TC) neurons to a standardized battery of current stimuli. Each current amplitude was normalized by the threshold current of each neuron (e.g. 150 % threshold, see Methods). Third row is a low-threshold burst response from a hyperpolarized holding potential, V_{hold} = −84 mV (burst mode), the other responses are elicited from a depolarized holding potential, V_{hold} = −64 mV (tonic mode). Two different holding currents (I_{hold} - tonic, I_{hold} - burst) are injected to obtain the desired V_{hold}. The vertical scale bar applies to all the traces, the first horizontal scale bar from the top refers to the first two rows, the second applies to the last four rows. (C) Analysis of adaptation index (AI) from recordings in

tonic mode. Solid line is a non-parametric estimation of the distribution, dashed lines are two Gaussian distributions fitted to the data (see Methods). The vertical line indicates the cut-off value.

Visual inspection of 50 reconstructed morphologies (24 from the VPL, 26 from the VPM nuclei) revealed variability in the number of principal dendritic trunks and their orientation, in agreement with previous anatomical studies (4).

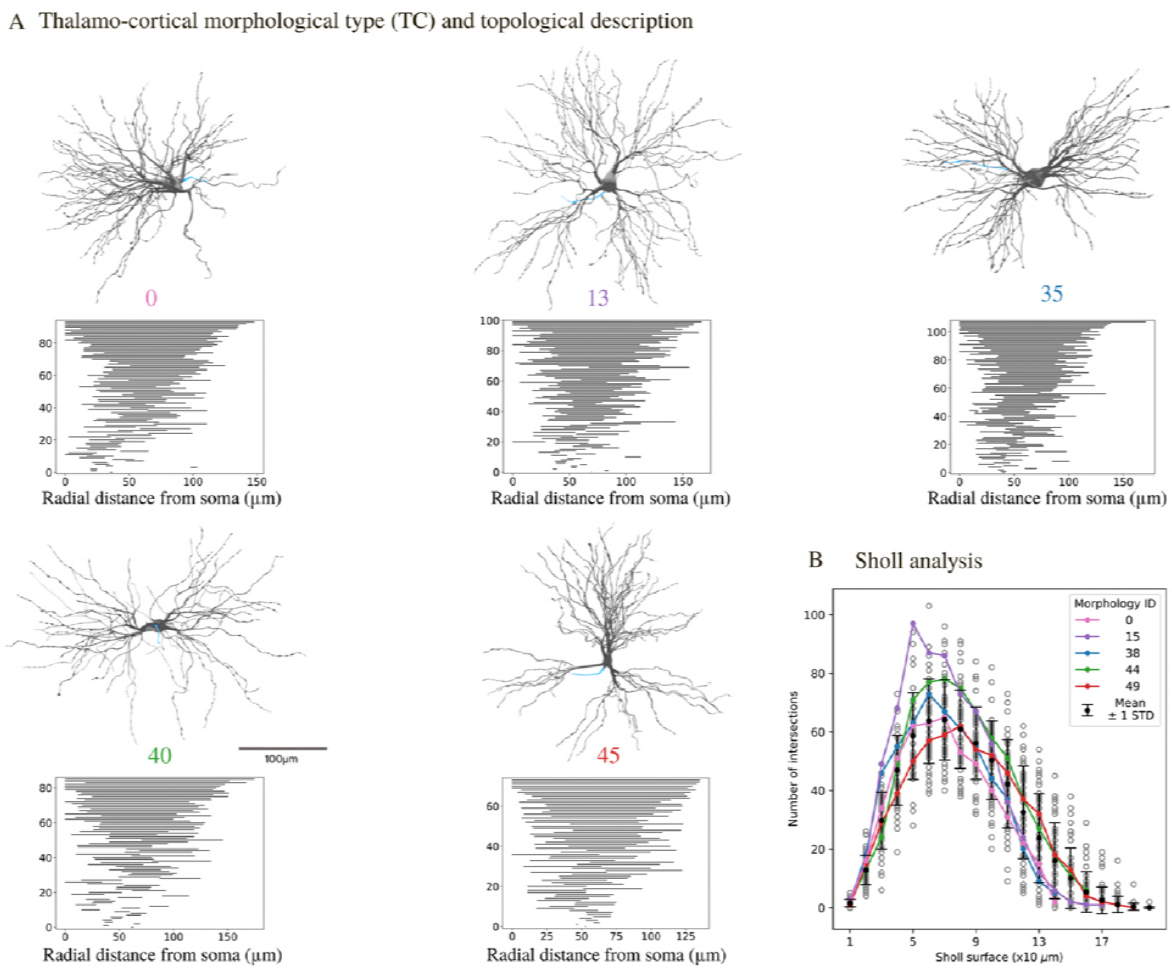

Figure 2: Morphological properties.

118 (A) Renderings of 3D reconstructed TC neurons along with their persistence barcode according
119 to (20). Grey: soma and dendrites, blue: axon only small sections available). The persistence
120 barcode is a topological description of the branching pattern of the neurons' dendrites. (B) Sholl
121 analysis of TC neuron dendrites. For each Sholl ring, the number of intersections is shown (mean
122 ± standard deviation, N = 50). Each grey circle represents one morphology, colored lines
123 correspond to the morphologies in A. See Fig S1 for further analysis.
124
125 The maximum radial extent of the dendrites ranged between 120 and 200 µm and they
126 started to branch between 20 and 50 µm from the soma (Fig S1). We then analyzed the
127 morphologies with two methods in order to quantitavely classify different morphological types.
128 We used algebraic topology to extract the persistent homology of each morphology and to
129 visualize the persistence barcode (20) (Fig 2A, see Methods). Each horizontal bar in the
130 persistence barcode represents the start and end point of each dendritic component in terms of
131 its radial distance from the soma. The barcodes of all the morphologies followed a semi-
132 continuous distribution of decreasing length. To quantify the differences between the barcodes,
133 we computed the pairwise distances of the persistence images (see Methods and Fig S1). We
134 found that they were in general small (<0.4, values expected to vary between 0 and 1). These
135 findings indicate that the morphologies cannot be grouped in different classes based on the
136 topology of their dendrites. Furthermore, we performed Sholl Analysis (21) to compare the
137 complexity of the dendritic trees (Fig 2B). We observed that all the morphologies had dense
138 dendritic branches, with a maximum number of 50-100 intersections between 50-80 µm from
139 the soma. When comparing the Sholl profiles for each pair of neurons we could not find any

140 statistically significant difference (Fig S1C). Considering the results of topological and Sholl
141 analyses, we grouped all the morphologies in one morphological type (m-type) called
142 thalamocortical (TC) m-type.

143 We used an adaptive stimulation protocol, called e-code, consisting of a battery of current
144 stimuli (e- code, see Methods for details), where the stimulation amplitude was adapted to the
145 excitability of different neurons. This standardized protocol has previously been used to build
146 biophysically-accurate models of cortical electrical types (e-types) (16). However, TC neurons
147 from different thalamic nuclei and species fire action potentials in two distinct firing modes,
148 namely tonic firing, when stimulated from a relatively depolarized membrane potential or low-
149 threshold bursting, from a hyperpolarized membrane potential (5). We thus extended the e-code
150 to include two different holding currents. All the neurons recorded in this study displayed tonic
151 and burst firing, when stimulated with the appropriate holding current (Fig 1). Moreover, we
152 were able to classify different e-types by considering the voltage traces recorded in tonic mode
153 in response to step current injections (Fig 1). The majority of the cells (59.3 %) showed a non-
154 adapting tonic discharge (continuous non-adapting low-threshold bursting, cNAD_ltb e-type)
155 while others (40.7 %) had higher adaptation rates (continuous non-adapting low-threshold
156 bursting, cAD_ltb e-type), as reflected by the adaptation index (Fig 1C). We followed the Petilla
157 convention (22) for naming the tonic firing discharge (cNAD or cAD), extending it to include "_ltb"
158 for the low-threshold bursting property. In some rare examples, we noticed acceleration in the
159 firing rate with decreasing inter-spike intervals (ISIs) towards the end of the stimulus. Similar
160 adapting and accelerating responses have already been described in the VB thalamus of the cat
161 (7). We also observed stereotypical burst firing responses within the same cell, with variation of

162 the number of spikes per burst in different cells, but the burst firing responses alone were
163 insufficient to classify distinct e-types.
164
165 **Constraining the models with experimental data**
166 Multi-compartmental models comes with the need of tuning a large number of parameters
167 (23), therefore we constrained the models as much as possible from experimental data. We first
168 combined the morphology and the ionic currents models in the different morphological
169 compartments (soma, dendrites and axon). Given that the reconstruction of the axon was
170 limited, we replaced it with a stub representing the initial segment (16). We used previously
171 published ionic current models and selected those that best matched properties measured in rat
172 TC neurons (see Methods). The kinetics parameters were not part of the free parameters of the
173 models. The distribution of the different ionic currents and their conductances in the dendrites
174 of TC neurons is largely unknown. The current amplitudes of the fast sodium, persistent and
175 transient (A-type) potassium currents were measured, but only up to 40-50 µm from the soma
176 (24). Indirect measures of burst properties (15) or Ca^{2+} imaging studies (25) suggest that the low-
177 threshold calcium (T-type) channels are uniformly distributed in the somatodendritic
178 compartments. We thus assumed different peak conductance in the soma, dendrites and axon
179 for all the ionic currents, except for I_{CaT}, which had the same conductance value in the soma and
180 dendrites. We then extracted the mean and standard deviation (STD) of different electrical
181 features in order to capture the variability of firing responses from different cells of the same e-
182 type (9) (Fig 3).
183

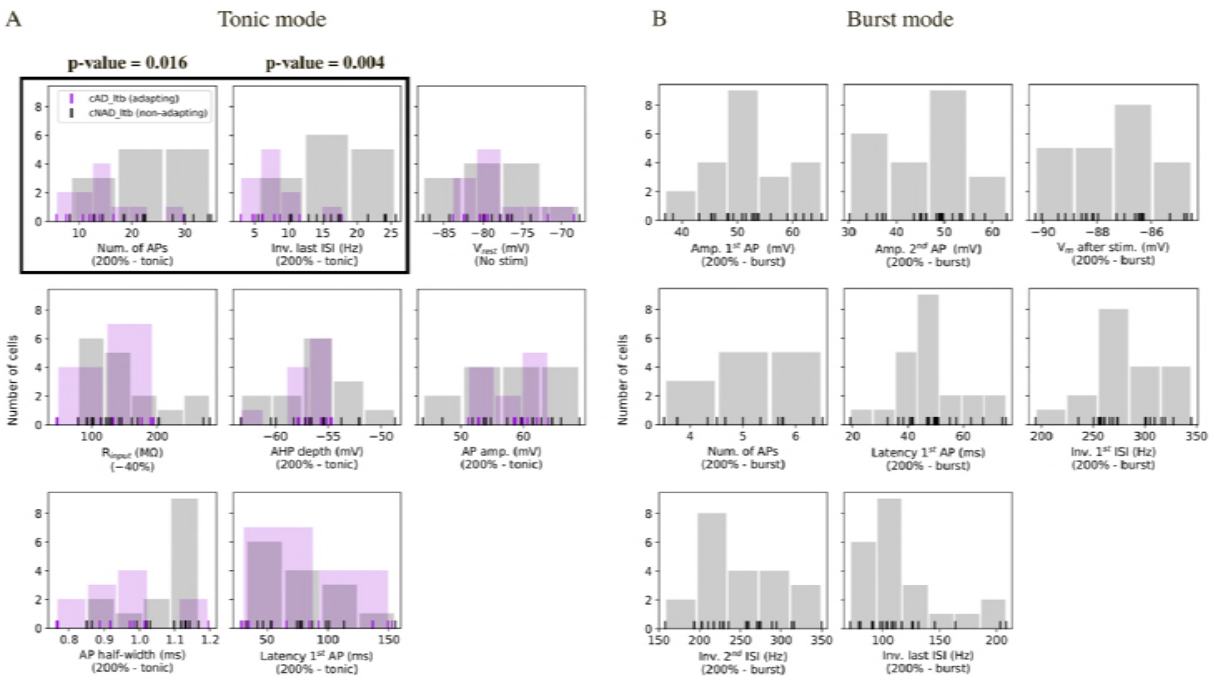

Figure 3: Histograms of electrical features.

Each vertical line represents the mean feature value for a cell. Tonic and burst refer to the holding voltage as in Fig 1. (A) Feature values extracted from recordings in tonic mode (N = 11 cAD_ltb cells, N = 16 cNAD_ltb cells). The features highlighted by a black box show different distributions for the cNAD_ltb and cAD_ltb electrical types (e-types) (p-value<0.05, two- sided Mann-Whitney U test with Bonferroni correction for multiple comparisons). Passive properties (V_{rest}, R_{input}) and spike shape features (AHP depth, AP amp., etc.) did not show clear differences between the two e-types. (B) Features measuring burst firing properties (N = 22 cells).

We observed that some features extracted from tonic firing responses had distinct distributions between the cAD_ltb and cNAD_ltb e-types (Fig 3A). The features were chosen in order to quantify salient physiological properties of TC neurons and to constrain the parameters

of the model, namely the peak conductance of each ionic current. The average value and STD of the features were used as optimization objective (multi-objective optimization, MOO). Twenty-five parameters were allowed to vary between the upper and lower bounds shown in Fig 5. The models were associated with a training error, i.e. a set of all the feature errors (measured as absolute z-scores) (9,18,26).

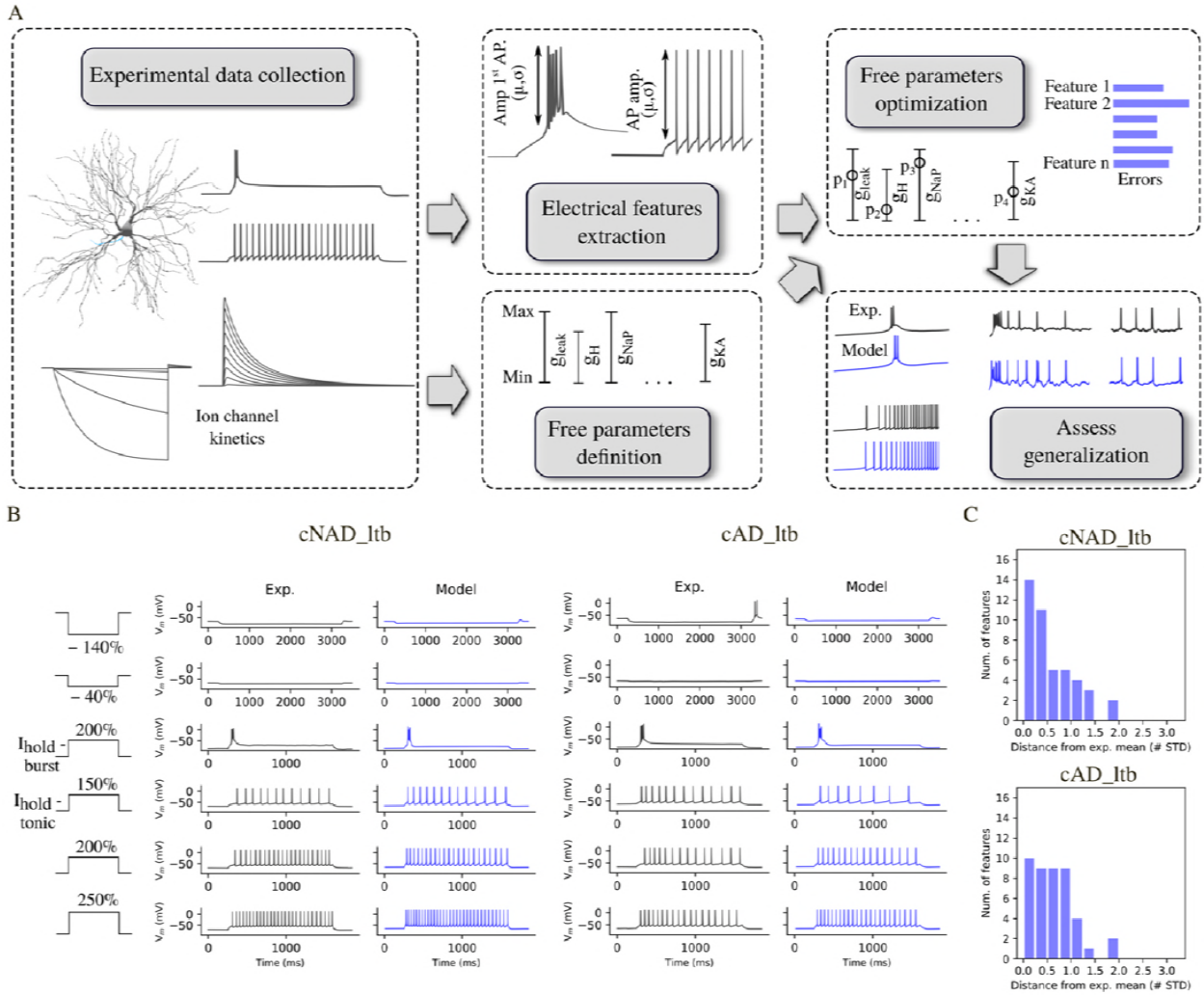

Figure 4: Models of different TC e-types and their fitting errors.

(A) Single neuron modelling pipeline. (B) Experimental and model voltage responses to a variety of stimuli pattern used during the optimization of cNAD_ltb and cAD_ltb e-types. (C) Feature errors of the models shown in (B) reported as deviation from the experimental mean. The models

are compared with the mean of features shown in Fig 3. Note that the models shown in B are fitted in order to reproduce the mean firing properties, not only a specific experimental recording. See Fig S2 for a complete list of fitting errors. By applying this MOO procedure, we generated multiple models with distinct parameter combinations that reproduced tonic and low-threshold burst firing in cNAD_ltb and cAD_ltb e-types (Fig 4).

Model and experimental diversity

We found that different sets of parameter values reproduced the target firing behavior (Fig 5B). We further analyzed models that had all the feature errors below 3 STD. Models' voltage responses reflected the characteristic firing properties of TC neurons (Fig S3), indicating that the selected set of features were sufficient to capture the two firing modes, in both the adapting and non-adapting e-types. The voltage traces from different models showed small differences in spike amplitude, firing frequency, and depth of the after-hyperpolarization, as reflected by the variability of features values (Fig 5C).

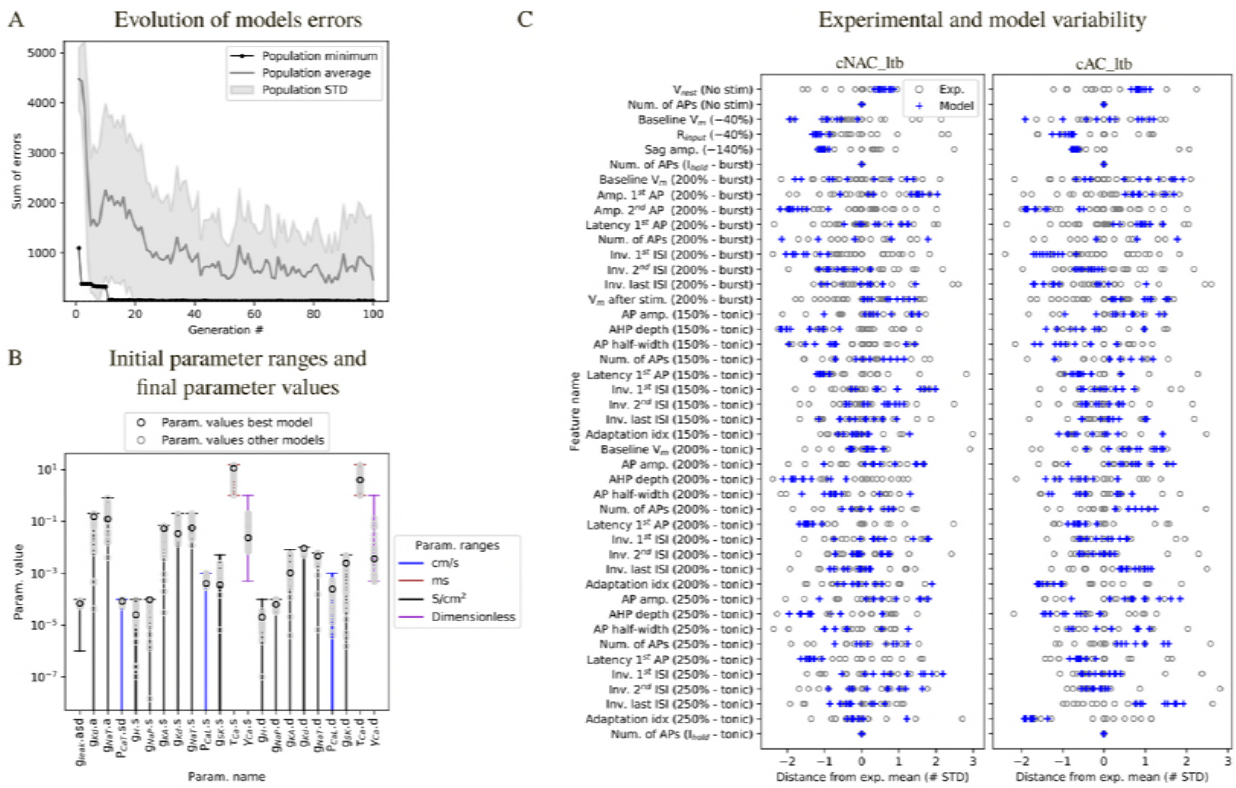

Figure 5: Diversity of model parameters and experimental variability.

(A) Example of model fitting errors (sum of all feature errors) during optimization. (B) Initial parameter ranges and diversity of solutions. Each vertical line represents the range for the parameters, when the horizontal lower bar is missing the bound is 0. The characters following "." in the parameter name specifies the morphological compartment for the parameter ("s": soma, "d": dendrites, "a": axon). Black circles: parameter values for one of the models in Fig 4, grey circles: parameter values of the models with all feature errors below 3 STD. (C) Features variability in the models and experiments. Blue crosses: feature errors of a sample of 10 models. Each grey circle is the z-scored feature value of one experimental cell, obtained from the feature values shown in Fig 3. The protocol names are shown in parenthesis and corresponds to the stimuli shown in Fig 1 and Fig 4, tonic and burst refer to the holding current as in Fig 1.

235 Spike-shape related features (e.g. AP. amplitude) in the different models covered the space
236 of the experimental variability, while for some features (e.g. input resistance, R_{input}), all models
237 tended to cluster on one of the tails of the experimental distribution. R_{input} relates to the neuron
238 passive properties and depends both on the number of channels open at rest (inverse of the leak
239 conductance in the model) and the size of the cell. Given that all the models were constrained
240 on a single morphology, this result is not surprising. The number of action potentials (Num. of
241 APs) in different conditions (No stim, I_{hold}) ensured that the models did not spike in the absence
242 of a stimulus or in response to the holding current. For this reason, all the experimental and
243 model feature values in 5C are equal to 0. Other features, such as latency to the first spike and
244 sag amplitude were less variable in the models compared to experiments. We hypothesized that
245 this depended on the variable stimulation amplitudes applied to different experimental cells,
246 while all the models were stimulated with the same current amplitudes.

247 We examined the diversity of the parameter values with respect to the initial parameter
248 range (Fig 5B). Most of the optimized parameter values spanned intervals larger than one order
249 of magnitude. On the other hand, some parameter values were restricted to one order of
250 magnitude, for example the permeability of the low-threshold calcium current P_{CaT}. This result is
251 in agreement with experiments showing a minimum value of I_{CaT} is critical to generate burst
252 activity and this critical value is reached only at a certain postnatal age (27). The value of P_{CaT} was
253 constrained by features measuring burst activity (such as number of spikes, frequency, etc.).

Assessment of model generalization

We used different stimuli for model fitting (current steps) and for generalization assessment (current ramps and noise). We simulated the experimental ramp currents in-silico, by stimulating the models with the appropriate holding currents for the two firing modes and a linearly increasing current. We first compared visually the model responses with the experimental recordings (Fig 6A).

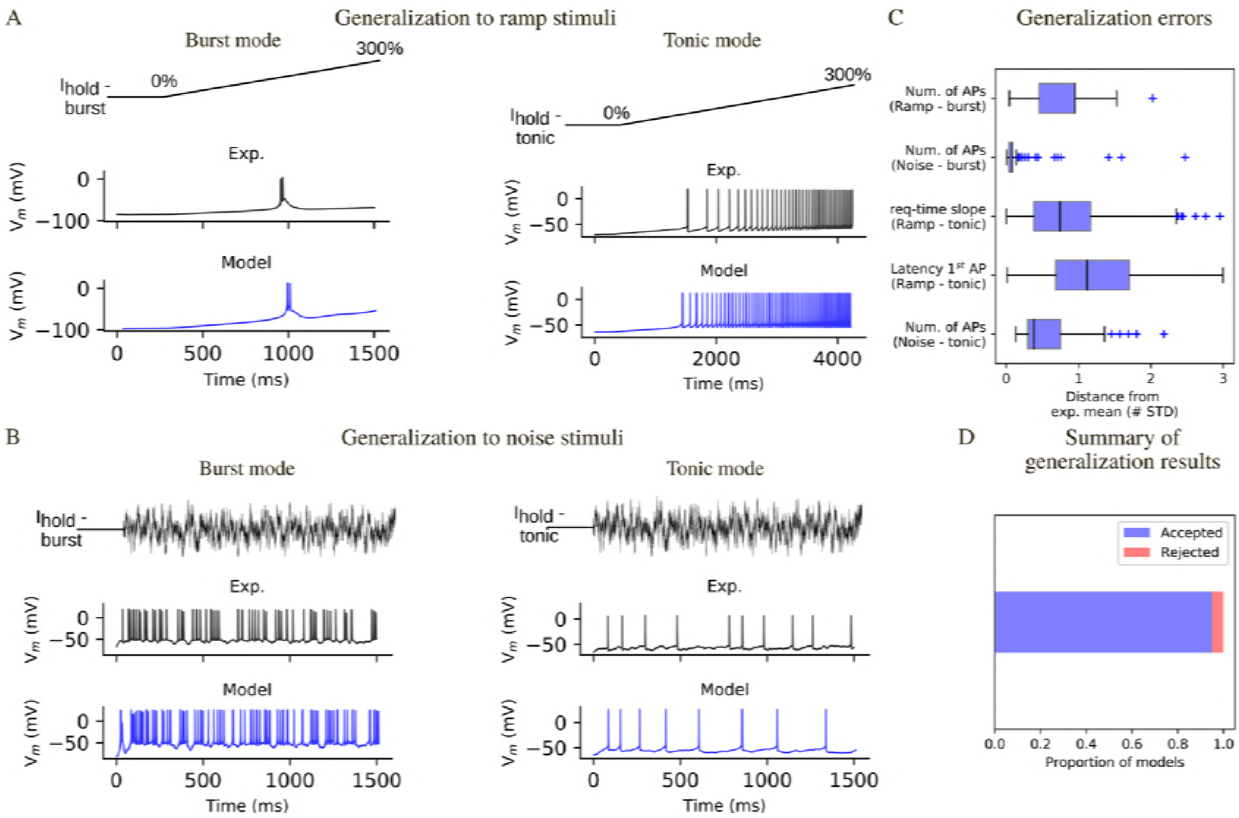

Figure 6: Model generalization.

(A) Responses to a ramp current injection in burst mode (left) and tonic mode (center). (B) Responses to a noise current generated according to an Ornstein-Uhlenbeck process and scaled based on the excitability of the different experimental cells and models (see Methods). (C) Generalization errors for all the models that passed the generalization test (all generalization

267 errors <3 STD). (D) Proportion of models that passed the generalization test (see Fig S4 for
268 examples of models that failed this test).
269
270 In burst mode, the models reproduced the different behaviors observed experimentally:
271 absence of a burst, small low-threshold spike, burst, burst followed by tonic firing (Fig S4).
272 Moreover, the latency of burst generation substantially overlapped with the experimental one.
273 However, a small fraction of models (1.2 %) generate repetitive burst that we have never
274 observed in the experimental recordings (Fig S4). These models were quantitatively rejected by
275 considering the number of spikes and the inter-spike intervals. In tonic mode, the latency to first
276 spike, the voltage threshold, the shape of the subsequent action potentials and the increase in
277 firing frequency were comparable with the experimental recordings (Fig 6A). In addition, we
278 quantified the generalization error to ramp stimuli (Fig 6C), by considering the latency to first
279 spike, firing frequency increase over time (tonic mode) or number of spikes (burst mode).
280 Although conductance-based models can be fit by using step and ramp currents (26), these
281 stimuli are different from synaptic inputs, which can be simulated by injecting noisy currents. To
282 test the response to such network-like input, we used a noisy current varying accordingly to an
283 Ornstein-Uhlenbeck (OU) process (28) to compare models' responses with the experimental
284 data. Each experimentally recorded cell was stimulated with the same OU input, scaled by a
285 factor *w*. Experimentally, *w* was calculated during the experiment by evaluating the responses to
286 previous stimuli. We developed a similar approach to generate the noise stimuli in silico (see
287 Methods). The noise current was injected on top of the holding currents used during the
288 optimization. We found that the models reproduced well the subthreshold potential, spike times

289 and the distribution of single spikes and bursts (Fig 6B). Moreover, we quantitatively evaluated
290 the generalization to the noise stimulus by extracting features (e.g. number of spikes) and
291 comparing them with the experimental mean.

292 We computed generalization errors for each model, which were calculated similarly to the
293 optimization errors (Fig 6C). We considered a model acceptable after generalization if it had all
294 generalization errors <3 STD and we found that the majority of the models (>90%) passed the
295 generalization test.

296

297 **Sensitivity of electrical features to small parameter perturbations**

298 We assessed the robustness of the models to small changes in their parameter values. To
299 that end, we varied each parameter at a time by a small amount (± 2.5 % of the optimized value)
300 and computed the values of the features. A sensitivity value of 2 between parameter *p* and
301 feature *y* means that a 3 % change in *p* caused a 6 % change in *f*. We ranked the parameters from
302 the most to the least influential and the features from the most sensitive to the least sensitive.

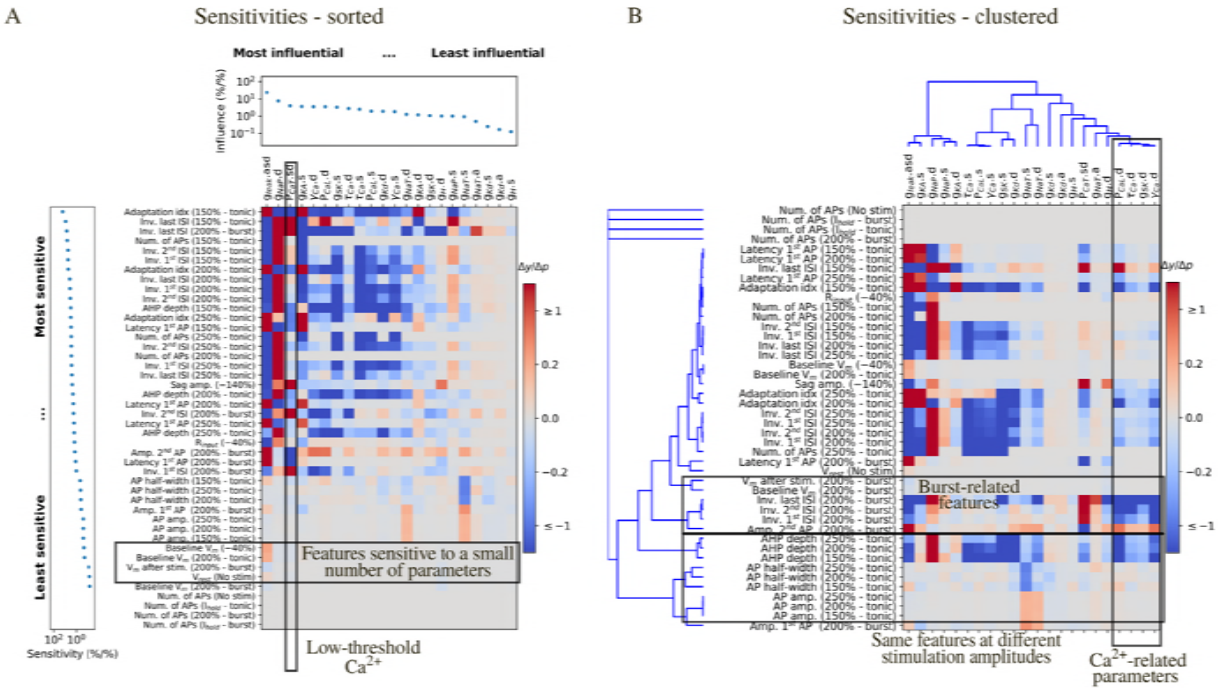

Figure 7: Local sensitivity analysis.

(A) Sensitivity of the feature values to small changes to the parameter values for the cAD_ltb model in Fig 4. Sensitivities (Δy/Δp) are color coded as a heat map. Features are ranked from the most to the least sensitive and parameters are ranked from the most to the least influential. The last three rows are features that ensure that the models were not firing without input or in the response to the holding current. Small changes to the parameter values are not expected to make the model firing and thus the sensitivity of these features is 0. (B) Same sensitivity values as in (a), with features and parameters clustered by similar sensitivity and influences.

The conductance of the leak current g_{leak} emerged as the most influential parameter (Fig 7A). An increase in g_{leak} caused a decrease in firing frequency (inverse of inter-spike intervals, ISIs) in both the tonic and burst firing modes. These results are easy to interpret when considering Ohm's law: increasing g_{leak} means decreasing the input resistance of the model, so that for the same input

317 current the voltage response becomes smaller. The second most influential parameter was the
318 conductance of the persistent sodium current g_{NaP} in the dendrites, which increased the tonic
319 firing rate as expected from a depolarizing current and had an effect on the late phase of the low-
320 threshold burst (inverse last ISI - burst). An increase in the permeability of the low-threshold
321 calcium current P_{CaT}, known to be one the main currents underlying low threshold bursting,
322 enhanced burst firing responses (it decreased the inverse of ISIs) and had effects on some of the
323 tonic features. P_{CaT} was the third most influential parameter. These findings show that I_{CaT} is the
324 main driver of the low-threshold burst, but other currents, such as I_{NaP} contributes as well.
325 Increasing the dendritic permeability of the high threshold calcium current P_{CaL} decreased the
326 tonic firing rate, despite being a depolarizing current. Increasing P_{CaL} means higher Ca^{2+} influx and
327 higher amplitude of the Ca^{2+}-activated potassium current (I_{SK}). The parameter g_{SK} had indeed a
328 similar effect on the features and thus clustered together with P_{CaL} (Fig 7B). Increasing the
329 conductance of the transient sodium conductance g_{NaT} increased action potential amplitude and
330 decreased its duration. Sag amplitude, that is known to depend on the activity of I_H, was mainly
331 influenced by change in g_{leak}, P_{CaT} and g_H. In summary, each parameter influenced at least one
332 feature. Some features were weakly influenced by small parameter changes, e.g. baseline
333 voltage, which depend more on the holding current amplitude, than on the model parameters.
334 These results indicate that the model ability to generate tonic and burst firing is robust to small
335 changes in parameter values and that all the parameters were constrained during the
336 optimization by one or more features.

337 We then analyzed which features depended similarly on parameter changes, as they may
338 add superfluous degrees of freedom during parameters search. Fig 7B shows the same

339 sensitivities as in Fig 7A, clustered by their similarities (see Methods). Features clustered together
340 if they were sensitive to similar parameter combinations and parameters clustered based on their
341 similar influence on the features. Not surprisingly, the same tonic features measured at different
342 level of current stimulation clustered together (e.g. AP amplitude and half-width, AHP depth,
343 latency of the first ISI) and tonic firing features belonged to a cluster that was different from burst
344 features.
345

346 **Preservation of model firing properties with different morphologies**

347 We optimized the parameters for the adapting and non-adapting e-models in combination with
348 two different experimental morphologies and then tested them with the other 48 morphologies.
349 Considering that morphologies could not be classified in different m-types based on topological
350 analysis of their dendrites and that TC neurons have been shown to be electrically compact (15),
351 we expected the electrical behavior to be conserved when changing morphology. Nonetheless,
352 different neurons vary in their input resistance R_{input} and rheobase current I_{thr} due to variation in
353 the surface area. Variation in R_{input} and I_{thr} made the current amplitude applied during the
354 optimization inadequate to generate the appropriate voltage trajectories. We thus devised an
355 algorithm to search for the holding current to obtain the target holding voltage (for example −64
356 mV or −84 mV for tonic and burst firing, respectively) and I_{thr} from the desired holding voltage.
357 The different e-model/morphology combinations (me-combinations) were evaluated by
358 computing the same feature errors calculated during optimization. For each morphology, we
359 selected the e-model that generated the smallest maximum error. All me-combinations
360 reproduced burst and tonic firing (Fig 8C). However, two me-combinations generated responses

with a small number of features that deviated from the experimental mean. We chose the value of 3 STD as a threshold to define which me-combinations were acceptable (29), yielding 48 acceptable me-combinations out of the 50 tested (Fig 8A). We analyzed more closely which features were significantly different from the experimental mean. In Fig 8B we show that the rejected me-combinations had too many action potentials in the burst.

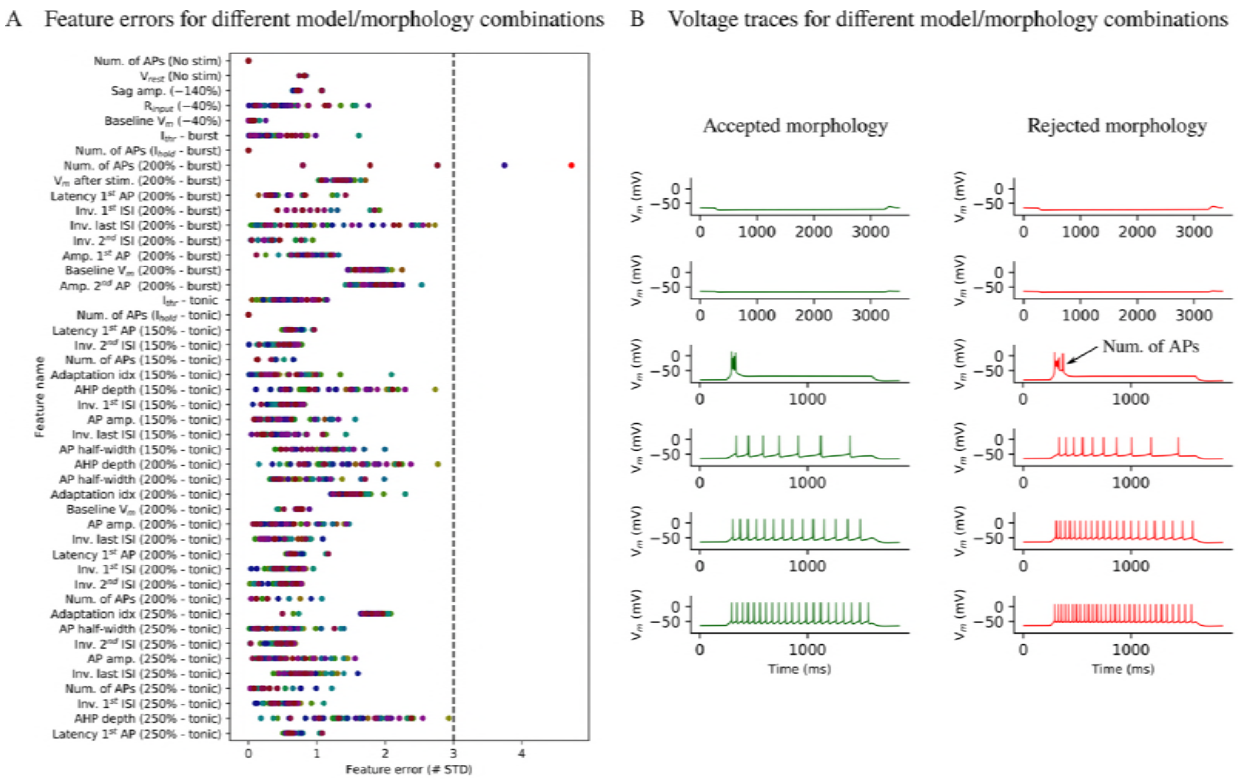

Figure 8: Model generalization to different experimental morphologies.

(A) Feature errors from the best electrical models (e-model) showed in Fig 4 applied to 50 different TC cell morphologies. Each morphology is represented with a different color. E-models/morphology combinations with at least one feature error > 3 STD (dashed line) were rejected. (B) Example of voltage responses from an accepted and from a rejected e-

373 model/morphology combination. Feature errors for the rejected combination are shown in red
374 in (A) and are indicated on the voltage trace.
375

376 **Discussion**

377 Our objective was to apply and extend an existing data-driven pipeline to identify the cell
378 types and build models of VB thalamocortical neurons that reproduce the multiple firing modes
379 that have been experimentally observed. We successfully modelled these novel firing types, by
380 including additional stimulation protocols and features to constrain the low-threshold burst.
381 Our morphological and electrical data were used to define the properties of VB TC neurons
382 in the rat. We found two electrical types (e-types) of TC neurons, but no objectively different
383 morphological types (m-types) were revealed either using Sholl analysis (21) or topological
384 analysis of dendritic branching (20). We cannot exclude that refinements to these methods will
385 reveal different m-types similar to the ones described in the visual thalamus of the mouse (30).
386 We also showed that automatic parameter search can be applied to build biophysically and
387 morphologically detailed models. This method was already applied to model canonical firing
388 behavior in cortical, hippocampal and cerebellar granule neurons (9,10,16,17,31,32). To the best
389 of our knowledge, such an automatic parameter search has not previously been used to capture
390 different firing modes and complex firing behavior such as low-threshold bursting in thalamic
391 neurons. Standardized electrophysiological protocols allowed us to identify for the first time in
392 juvenile rat adapting and non-adapting e-types of TC VB neurons that were previously observed
393 in other species (7). This finding suggests that the intrinsic properties of TC neurons contribut to
394 adaptation, a key phenomenon for filtering out irrelevant stimuli, before sensory information

395 reaches the neocortex. Further experiments are needed to elucidate the relative contribution of
396 intrinsic mechanisms and network properties to adaptation in somatosensory systems. We
397 named the two main e-types continuous non-adapting low-threshold bursting (cNAD_ltb) and
398 continuous adapting low-threshold bursting (cAD_ltb) by following and extending existing
399 conventions (16,22,31).

400 In this study, we improved upon previous morphologically and biophysically detailed
401 models of tonic and burst firing in TC neurons (12,13,15) by explicitly constraining the parameters
402 with experimental data, without hand-tuning of parameter values. Unlike previous models, we
403 chose a multi-objective optimization for a methodological and a scientific reason: it is more time-
404 efficient, reproducible, and it approximates the variability in ionic channel expression of
405 biological neurons (31,33–35), as shown by the family of acceptable solutions we found.
406 However, experiments aimed at quantifying ion channel conductances are essential to assess if
407 these solutions fall between biological ranges. Furthermore, we tested the generalization
408 capability of the models and found that more than 90% of the models were comparable with the
409 experimental data.

410 Nonetheless, we noticed some inaccuracies when comparing the voltage traces with the
411 experimental data when assessing the generalization of some models. For instance, some models
412 tended to generate small transient oscillations in response to ramp stimuli in burst mode. This
413 result is not surprising, considering that the exact kinetics for all the ionic currents are not
414 available and that there are known limitations in models of ionic channels derived from the
415 literature or from other models (36,37). In particular, modifications of the kinetics of the low-

416 threshold calcium current was shown to explain the propensity to generate oscillatory bursts in
417 TC neurons of other nuclei and species (38).

418 TC neurons have been shown to be electrically compact (15) and could, in principle, be
419 modeled as a single compartment. However, active mechanisms need to be located in the
420 dendrites in order to ensure synaptic integration and amplification (39). Information regarding
421 specific conductances or firing properties in the dendrites of TC neurons is limited. For this
422 reason, dendritic parameters in our models may be underconstrained. However, the sensitivity
423 analysis (see below) revealed that dendritic parameters did not appear to be the least
424 constrained because they influenced different tonic and burst-related features.

425 We included in the model fitting and validation pipeline a sensitivity analysis, which is often
426 neglected in computational neuroscience (40). Although we cannot use our simple univariate
427 approach to explore multidimensional parameter correlations and principles of co-regulation of
428 ion channels expression, it is useful to find better constraints for parameters optimization. The
429 selection of the features is indeed a step that still requires care and experience by modelers.
430 Furthermore, this type of sensitivity analysis allows to identify parameters that can be traded-off
431 during the optimization and that can be removed in order to reduce the dimensionality of the
432 problem. In our study, four parameters related to the calcium dynamics were shown to influence
433 the features in a very similar fashion. This type of analysis is of particular importance in future
434 work aimed at using the full diversity of ion channels that can be inferred from gene expression
435 data. More in detail, we propose that sensitivity analysis should be a fundamental tool in
436 selecting which conductances are successfully optimized by the available experimental
437 constraints. The example we showed is a local approach, applied to a specific solution to the

438 optimization problem, which showed that our models are robust to small parameter changes.
439 This analysis can be extended to study how the sensitivities vary in the neighborhood of different
440 solutions.

441 In conclusion, we systematically studied the morphological and electrical properties of VB
442 TC neurons and used these experimental data to constrain single neuron models, test their
443 generalization capability and assess their robustness. Further work will validate these models in
444 response to synaptic activity, in order to include them in a large-scale model of thalamocortical
445 microcircuitry (16).

446

447 ## Methods

448 **Experimental procedures**

449 Experimental data were collected in conformity with the Swiss Welfare Act and the Swiss
450 National Institutional Guidelines on Animal Experimentation for the ethical use of animals. The
451 Swiss Cantonal Veterinary Office approved the project following an ethical review by the State
452 Committee for Animal Experimentation.

453 All the experiments were conducted on coronal or horizontal brain slices (300 µm thick-
454 ness) from the right hemisphere of male and female juvenile (P14-18) Wistar Han rats. The region
455 of interest was identified using the Paxinos and Watson rat brain atlas (19). After decapitation,
456 brains were quickly dissected and sliced (HR2 vibratome, Sigmann Elektronik, Germany) in ice-
457 cold standard ACSF (in mM: NaCl 125.0, KCl 2.50, $MgCl_2$ 1.00, NaH_2PO_4 1.25, $CaCl_2$ 2.00, D-(+)-
458 Glucose 50.00, $NaHCO_3$ 50.00; pH 7.40, aerated with 95% O_2 / 5% CO_2). Recordings of

459 thalamocortical neurons in the VB complex were performed at 34 °C in standard ACSF with an
460 Axon Instruments Axopatch 200B Amplifier (Molecular Devices, USA) using 5–7 MΩ borosilicate
461 pipettes, containing (in mM): K^+-gluconate 110.00, KCl 10.00, ATP-Mg^{2+} 4.00, Na_2-
462 phosphocreatine 10.00, GTP-Na^+ 0.30, HEPES 10.00, biocytin 13.00; pH adjusted to 7.20 with
463 KOH, osmolarity 270-300 mOsm. Cells were visualized using infrared differential interference
464 contrast video microscopy (VX55 camera, Till Photonics, Germany and BX51WI microscope,
465 Olympus, Japan).

466 Membrane potentials were sampled at 10 kHz using an ITC-18 digitizing board (InstruTECH,
467 USA) controlled by custom-written software operating within IGOR Pro (Wavemetrics, USA).
468 Voltage signals were low-pass filtered (Bessel, 10 kHz) and corrected after acquisition for the
469 liquid junction potential (LJP) of −14 mV. Only cells with a series resistance <25 MΩ were used.

470 After reaching the whole-cell configuration, a battery of current stimuli was injected into
471 the cells and repeated 2-4 times (e-code). During the entire protocol, we defined offset currents
472 in order to keep the cell at −50 mV (tonic firing) or −70 mV (burst firing) before LJP correction and
473 applied them during the entire protocol. The step and ramp currents were injected with a delay
474 of 250 ms in the experiment. In the models, the stimuli were injected with a delay of 800 ms, to
475 allow for the decay of transients due to initialization. Each stimulus was normalized to the
476 rheobase current of each cell, calculated on-line as the current that elicited one spike (stimulus
477 TestAmp, duration 1350 ms). The stimuli used for in the experiments, for fitting and testing the
478 models were:

479 - IDRest: current step of 1350 ms, injected at different amplitude levels in 25 % increments
480 (range 50-300 % threshold). IDRest was renamed to Step in the model.

481 • IDThresh: current step with duration of 270 ms, 4 % increments (range 50 - 130 %).

482 • IV: hyperpolarizing and depolarizing steps of 3000 ms injected in 20 % increments (range
483 −140 - 60%).

484 • SponNoHold: the first 10 seconds of this stimulus was used to calculate the resting
485 membrane potential. No holding or stimulation currents were applied.

486 • SponHold: the first 10 seconds of this stimulus was used to calculate the holding current
487 applied to keep the cells at the target potential.

488 • PosCheops: ramps of current from 0 to 300 % and from 300 to 0 % having progressively
489 shorter durations (4000 ms, 2000 ms, 1250 ms). To test the models in tonic mode we used
490 the first increasing ramp in the stimulus, while we used the last one in the bursting firing
491 mode. We chose the last one because the biological cells were more likely to generate a
492 burst.

493 • NOISEOU3: the original wave was scaled and offset for each cell based on the spike
494 frequency responses to IDRest responses. The scaling factor *w* was extracted from the
495 frequency-current curve and corresponded to the current value that made the cell fire at
496 7.5 Hz.

497 Neurons that were completely stained and those with high contrast were reconstructed in
498 3D and corrected for shrinkage as previously described (41). Reconstruction used the
499 Neurolucida system (MicroBrightField). The location of the stained cells was defined by
500 overlaying the stained slice and applying manually an affine transformation to the Paxinos and
501 Watson's rat atlas (19).

502 **Electrical features extraction**

503 Electrical features were extracted using the Electrophys Feature Extraction Library (eFEL)
504 (42). We calculated the adaptation index (AI) from recordings in tonic mode (Step 200 %
505 threshold) and classified TC VB neurons into adapting (AI>=0.029) and non-adapting (AI<0.029)
506 electrical types. AI was calculated using the eFEL feature *adaptation_index2* and corresponded
507 to the average of the difference between two consecutive inter-spike intervals (ISI) normalized
508 by their sum. The cut-off value was calculated after fitting a Gaussian mixture model to the
509 bimodal data, using available routines for R (43,44). In order to group data from different cells
510 and generate population features, we normalized all the stimuli by the rheobase current I_{thr} of
511 each cell. To calculate I_{thr}, we used IDRest and IDThresh and selected the minimal amplitude that
512 evoked a single spike. The extracted features quantified passive (input resistance, resting
513 membrane potential), burst and tonic firing properties (number of spikes, inverse of inter-spike
514 intervals, latency to first spike), action potentials shape (amplitude, half-width, depth of the fast
515 after-hyperpolarization). We aimed at finding the minimal set of features that capture the most
516 important properties. This set was a trade-off between comprehensively describing the
517 experimental data (i.e. extracting all possible features), which can lead to over-fitting and loss of
518 generalizability, and a too small set that would miss some important characteristics. For the tonic
519 firing responses, we used three stimulation amplitudes (150 %, 200 %, 250 % of firing threshold)
520 which have been shown to reproduce the complete input-output function of the neurons (17,41).
521 Responses to two hyperpolarizing steps of different amplitudes (−40 % and −140 % threshold)
522 constrained the input resistance and the conductance of currents activated in hyperpolarization
523 (*sag_amplitude* feature). We included baseline voltage values in the optimization objectives to

524 ensure that the model was in the right firing regime and spike count to penalize models that were
525 firing in response to the holding currents. Along with the voltage features, we extracted mean
526 holding and threshold current values for all the experimental stimuli. Description of the features
527 and the details on their calculation are available on-line [49]. Current stimuli applied during the
528 optimization and generalization were directly obtained from the experimental values or
529 automatically calculated by following the experimental procedures (e.g. noise stimulus).

530 **Morphology analysis**

531 Reconstructed morphologies were analyzed to objectively identify different morphological
532 types. The Sholl profiles of each pair of cells was statistically tested by using k-samples Anderson-
533 Darling statistics. This test was preferred to the most common Kolmogorov- Smirnov test,
534 because it does not assume that the samples are drawn from a continuous distribution. The
535 different Sholl profiles are indeed an analysis of the intersections with discrete spheres.

536 To compare the topological description of each morphology we transformed the
537 persistence barcodes into persistence images and calculated their distances as in (20). Briefly, we
538 converted the persistence barcode, which encodes the start and end radial distances of a branch
539 in the neuronal tree, into a persistence diagram. In the persistence diagram, each bar of the
540 barcode is converted into a point in a 2D space, where the X and Y coordinates are the start and
541 end radial distances of each bar. The persistence diagram was then converted in a persistence
542 image by applying a Gaussian kernel. We used the library NeuroM (45) to perform Sholl and
543 morphometrics analyses. The reconstructed morphologies will be made publicly available on
544 neuromorpho.org.

545 **Ionic currents models**

546 We used Hodgkin-Huxley types of ionic current models, starting from kinetics equations
547 already available in the neuroscientific literature. Along with kinetics of the ionic currents, we
548 stored information on the experimental conditions, such as temperature and LJP, by using the
549 software NeuroCurator (46). Whenever the data was available, we compared simulated voltage-
550 clamp experiments to experimental data from juvenile rats. Ionic currents I_i were defined as
551 functions of the membrane potential v, its maximal conductance density g_i and the constant
552 value of the reversal potential E_i:

553 $$I_i = g_i m_i^x h_i^y (v - E_i)$$

554 m_{ion} and h_{ion} represent activation and inactivation probability (varying between 0 and 1), with
555 integer exponents x and y. Each probability varied according to:

556 $$n^{'}(v) = (n_\infty(v) - n)/\tau_n(v)$$

557 where $n_\infty(v)$ is a function of voltage that represents the steady-state activation/inactivation
558 function (normally fitted with a Boltzmann curve) and $\tau_n(v)$ is a voltage-dependent time constant.
559 Exceptions to this formalism are ionic currents that do not inactivate (y = 0) and ionic currents
560 with (in)activation processes mediated by two or more time constants. Calcium currents (I_{CaT} and
561 I_{CaL}) were modeled according to the Goldman-Hodgkin-Katz constant field equation and had
562 permeability values instead of conductance (47).

563 **Fast transient sodium current I_{NaT} and delayed potassium current I_{Kd}.** I_{NaT} and I_{Kd} were
564 taken from a previous models of rat TC neurons from the VB nucleus (12), available on SenseLab
565 ModelDB (accession no. 279). I_{NaT} was compared with recordings of transient sodium currents in
566 P7-11 rat neurons from the dorsolateral geniculate (dLGN) nucleus (48).

567 **Low-threshold activated (T-type) calcium current I_{CaT}.** I_{CaT} model was taken from (12) and
568 available on-line (ModelDB, accession no. 279). This model was based on data recorded from VB
569 neurons of Sprague-Dawley rats (P7-12) at room temperature and corrected for −9 mV LJP (11).

570 **Hyperpolarization-activated cationic current I_H.** The steady-state activation for I_H was
571 derived from VB thalamic neurons in P10-20 Long-Evans rats and was already corrected for −10
572 mV LJP in the original publication (49). The equation used was:

573 $$m_\infty = 1/(1 + \exp[(v + 86.4)/11.2])$$

574 The time constant of activation was modeled as in (50), which derived a mathematical
575 description of I_H based on data from the dLGN in adult guinea pigs, recorded at 35.5 °C (51). The
576 equation describing the time dependence of activation was not corrected for simulations at
577 different temperatures and was:

578 $$\tau_m = 1/[\exp(-14.59 - 0.086v) + exp(-1.87 + 0.0701v)]$$

579 The equilibrium potential of the channel E_H was −43 mV. In silico voltage-clamp
580 experiments were compared with data in (49).

581 **Persistent sodium current I_{NaP}.** We modeled I_{NaP} as in (17) which based their model on
582 recordings from entorhinal neurons of Long-Evans rats (P25-P35) (52). The steady-state
583 activation was modified according to (48) and the steady-state inactivation according to (14). The
584 original steady-state activation data were recorded at room temperature (22-24°) and corrected
585 for −6/−7 mV LJP. Limited data on I_{NaP} are available from dissociated neurons from the dLGN
586 nucleus in Wistar rats (48).

587 **Fast transient (A-type) potassium current I_{KA}.** The mathematical formulation of I_{KA} was
588 based on data recorded from VB neurons in Sprague-Dawley rats (P7-15), recorded at room

589 temperature (22-24 °C) (53). A Q_{10} = 2.8 was experimentally determined and used for simulations
590 at different temperatures. In the original experiments a small LJP (<−4 mV) was measured and
591 not corrected. The current had a rapid and a slow component, represented by two activation and
592 two inactivation variables. The model of this current was provided by the authors of (14).

593 **High-threshold (L-type) calcium current I_{CaL}.** I_{CaL} model is the same as TC neurons model
594 previously published (14,50). The model was based on data from isolated guinea-pig
595 hippocampal neurons, recorded at room temperature (20-22 °C) with modifications to the
596 Boltzmann curve parameters of activation contained in the correction to the original models [59].
597 A small LJP (<3 mV) was not corrected (50). A Q_{10} = 3 was used for simulations at different
598 temperatures.

599 **Calcium-activated potassium currents.** TC neuron express genes for BK-type (54) and SK-
600 type calcium-activated potassium channels (55). Models of BK-type currents, similar to the I_C
601 current, have already been used to model TC neurons (14,50,54). However, data characterizing
602 this current in mammalian neurons are not available. We thus included only a model of I_{SK}
603 (available in ModelDB, accession no. 139653) based on rat mRNA expression data in Xenopus
604 oocytes (56).

605 **Intracellular calcium dynamics.** A simple exponential decay mechanism was used to model
606 the intracellular calcium dynamics (ModelDB, accession no. 139653). Both I_{CaT} and I_{CaL}
607 contributed to the intracellular calcium concentration.

608 In addition, we included a voltage-insensitive membrane current I_{leak}. The equilibrium
609 potential was −79 mV and corresponded to the average resting potential from our experimental
610 recordings.

611 **Simulation and parameters optimization**

612 NEURON 7.5 software was used for simulation (57). We used NEURON variable time step
613 method for all simulations. For the sake of spatial discretization, each section was divided into
614 segments of 40 µm length. The following global parameters were set: initial simulation voltage
615 (−79 mV), simulation temperature (34 °C), specific membrane capacitance (1 µF/cm^2), specific
616 intracellular resistivity 100 Ωcm for all the sections, equilibrium potentials for sodium and
617 potassium were 50 mV and −90 mV, respectively.

618 BluePyOpt (18) with Indicator Based Evolutionary Algorithm (IBEA) were used to fit the
619 models to the experimental data. Each optimization run was repeated with three different
620 random seeds and evaluated 100 individuals for 100 generations. The evaluation of these 300
621 individuals for 100 generations was parallelized using the *iPython ipyparallel* package and took
622 between 21 and 52 h on 48 CPU cores (Intel Xeon 2.60 GHz) on a computing cluster. Each
623 optimization run typically resulted in tens or hundreds of unique acceptable solutions, defined
624 as models having all feature errors below 3 STD from the experimental mean.

625 The models will be made publicly available at ModelDB (58). The configuration files for the
626 optimization and analysis will be made publicly available on Github, Bluepyopt page (59).

627 **Sensitivity analysis**

628 We performed a sensitivity analysis of an optimization solution by varying one parameter
629 value (p_m) at a time and calculating the electrical features from the voltage traces (y^+ and y^-). We
630 defined the sensitivity as the ratio between the normalized feature change and the parameter
631 change, which for smooth functions approximates a partial derivative (60,61). The features
632 changes were normalized by the optimized feature value. For small changes of parameter values,

we assumed that the features depend linearly on its parameters. We could thus linearize the relationship between the features and the parameters around an optimized parameter set and calculate the derivatives. The derivatives were calculated with a central difference scheme (60).

$$\frac{\partial y_n}{\partial p_m} \approx \frac{y_n^+ - y_n^-}{2\Delta p_m}$$

We collected the derivatives (sensitivities) in the *N X M* Jacobian matrix, with *N* representing the number of features and *M* the number of parameters.

To rank parameters and features we computed their relative importance by calculating their norms (the square root of the summed squared values) from the Jacobian columns and rows, respectively. To cluster parameters based on similar influences on the features and to cluster features that were similarly dependent on the parameters, we used angles between columns (or rows) to compute distances *D* between parameters (or features):

$$D = 1 - |\cos\theta|$$

Features where thus considered similar if they depended in a similar manner on the parameters, independent of sign or magnitude.

Acknowledgements

We thank the Blue Brain Project Visualization Team for generating the meshes and visualizing the 3D morphologies.

Author Contributions

Conceptualization: E.I., S.L.H. **Data Acquisition and Curation:** J.Y., Y.S. **Formal Analysis**: E.I., J.Y., B.Z., C.O. **Funding Acquisition**: S.L.H., H.M. **Investigation**: E.I., J.Y., Y.S. **Methodology**: E.I., B.Z.,

C.R., W.V. **Project Administration:** C.O., S.L.H., H.M. **Resources and Software**: J.Y., Y.S., B.Z., W.V., C.R. **Supervision**: S.L.H., H.M. **Validation and Visualization**: E.I. **Writing – Original Draft Preparation**: E.I. **Writing – Review & Editing**: E.I., J.Y., C.O., W.V., H.M., S.L.H.

Supporting Information captions

S1 Features Dataset – Electrical features

Spreadsheet containing experimental electrical figures, separated in three different sheets. The features, their means and standard deviations are used in Fig 1C, Fig 2, Fig 3, Fig 4C, Fig 5C, Fig 8A.

S2 Supporting figures

663 **References**

664 1. Sherman SM. The thalamus is more than just a relay. Current opinion in neurobiology.
665 2007;17(4):417–422.

666 2. Francis JT, Xu S, Chapin JK. Proprioceptive and cutaneous representations in the rat ventral
667 posterolateral thalamus. Journal of neurophysiology. 2008;99(5):2291–2304.

668 3. Jones E. The thalamus 2nd ed. Cambridge University Press Cambridge, UK; 2007.

669 4. McAlliser J, Wells J. The structural organization of the ventral posterolateral nucleus in the
670 rat. Journal of Comparative Neurology. 1981;197(2):271–301.

671 5. Llinás R, Jahnsen H. Electrophysiology of mammalian thalamic neurones in vitro. Nature.
672 1982;297(5865):406.

673 6. Jahnsen H, Llinas R. Electrophysiological properties of guinea-pig thalamic neurones: an in
674 vitro study. The Journal of physiology. 1984;349(1):205–226.

675 7. Turner JP, Anderson CM, Williams SR, Crunelli V. Morphology and membrane properties of
676 neurones in the cat ventrobasal thalamus in vitro. The Journal of Physiology.
677 1997;505(3):707–726.

678 8. Connelly WM, Crunelli V, Errington AC. Variable action potential backpropagation during
679 tonic firing and low-threshold spike bursts in thalamocortical but not thalamic reticular
680 nucleus neurons. Journal of Neuroscience. 2017;0015–17.

681 9. Druckmann S, Banitt Y, Gidon AA, Schürmann F, Markram H, Segev I. A novel multiple
682 objective optimization framework for constraining conductance-based neuron models by
683 experimental data. Frontiers in neuroscience. 2007;1:1.

684 10. Gouwens NW, Berg J, Feng D, Sorensen SA, Zeng H, Hawrylycz MJ, et al. Systematic
685 generation of biophysically detailed models for diverse cortical neuron types. Nature
686 communications. 2018;9(1):710.

687 11. Huguenard JR, McCormick DA. Simulation of the currents involved in rhythmic oscillations in
688 thalamic relay neurons. Journal of neurophysiology. 1992;68(4):1373–1383.

689 12. Destexhe A, Neubig M, Ulrich D, Huguenard J. Dendritic low-threshold calcium currents in
690 thalamic relay cells. Journal of Neuroscience. 1998;18(10):3574–3588.

691 13. Rhodes PA, Llinás R. A model of thalamocortical relay cells. The Journal of physiology.
692 2005;565(3):765–781.

693 14. Amarillo Y, Zagha E, Mato G, Rudy B, Nadal MS. The interplay of seven subthreshold
694 conductances controls the resting membrane potential and the oscillatory behavior of
695 thalamocortical neurons. Journal of Neurophysiology. 2014;112(2):393–410.

696 15. Connelly WM, Crunelli V, Errington AC. The global spike: conserved dendritic properties
697 enable unique Ca2+ spike generation in low-threshold spiking neurons. Journal of
698 Neuroscience. 2015;35(47):15505–15522.

16. Markram H, Muller E, Ramaswamy S, Reimann MW, Abdellah M, Sanchez CA, et al. Reconstruction and Simulation of Neocortical Microcircuitry. Cell. 2015;163(2):456–492.

17. Hay E, Hill S, Schürmann F, Markram H, Segev I. Models of neocortical layer 5b pyramidal cells capturing a wide range of dendritic and perisomatic active properties. PLoS computational biology. 2011;7(7):e1002107.

18. Van Geit W, Gevaert M, Chindemi G, Rössert C, Courcol J-D, Muller EB, et al. BluePyOpt: leveraging open source software and cloud infrastructure to optimise model parameters in neuroscience. Frontiers in neuroinformatics. 2016;10:17.

19. Paxinos G, Watson C. The rat brain atlas in stereotaxic coordinates. San Diego: Academic. 1998;

20. Kanari L, D\lotko P, Scolamiero M, Levi R, Shillcock J, Hess K, et al. A topological representation of branching neuronal morphologies. Neuroinformatics. 2018;16(1):3–13.

21. Sholl DA. Dendritic organization in the neurons of the visual and motor cortices of the cat. Journal of anatomy. 1953;87(Pt 4):387.

22. Ascoli G a, Alonso-Nanclares L, Anderson S a, Barrionuevo G, Benavides-Piccione R, Burkhalter A, et al. Petilla terminology: nomenclature of features of GABAergic interneurons of the cerebral cortex. Nature reviews Neuroscience. 2008;9(7):557–568.

23. Almog M, Korngreen A. Is realistic neuronal modeling realistic? Journal of neurophysiology. 2016;116(5):2180–2209.

718 24. Williams SR, Stuart GJ. Action potential backpropagation and somato-dendritic distribution
719 of ion channels in thalamocortical neurons. Journal of Neuroscience. 2000;20(4):1307–1317.

720 25. Errington AC, Renger JJ, Uebele VN, Crunelli V. State-dependent firing determines intrinsic
721 dendritic Ca2+ signaling in thalamocortical neurons. Journal of Neuroscience.
722 2010;30(44):14843–14853.

723 26. Druckmann S, Berger TK, Hill S, Schürmann F, Markram H, Segev I. Evaluating automated
724 parameter constraining procedures of neuron models by experimental and surrogate data.
725 Biological cybernetics. 2008;99(4–5):371.

726 27. Velazquez JLP, Carlen PL. Development of firing patterns and electrical properties in neurons
727 of the rat ventrobasal thalamus. Developmental brain research. 1996;91(2):164–170.

728 28. Pozzorini C, Mensi S, Hagens O, Naud R, Koch C, Gerstner W. Automated high-throughput
729 characterization of single neurons by means of simplified spiking models. PLoS computational
730 biology. 2015;11(6):e1004275.

731 29. Hay E, Schürmann F, Markram H, Segev I. Preserving axosomatic spiking features despite
732 diverse dendritic morphology. Journal of neurophysiology. 2013;109(12):2972–2981.

733 30. Krahe TE, El-Danaf RN, Dilger EK, Henderson SC, Guido W. Morphologically distinct classes of
734 relay cells exhibit regional preferences in the dorsal lateral geniculate nucleus of the mouse.
735 Journal of Neuroscience. 2011;31(48):17437–17448.

736 31. Migliore R, Lupascu CA, Bologna LL, Romani A, Courcol J-D, Antonel S, et al. The physiological
737 variability of channel density in hippocampal CA1 pyramidal cells and interneurons explored
738 using a unified data-driven modeling workflow. PLoS computational biology.
739 2018;14(9):e1006423.

740 32. Masoli S, Rizza MF, Sgritta M, Van Geit W, Schürmann F, D'Angelo E. Single neuron
741 optimization as a basis for accurate biophysical modeling: the case of cerebellar granule cells.
742 Frontiers in cellular neuroscience. 2017;11:71.

743 33. Schulz DJ, Goaillard J-M, Marder E. Variable channel expression in identified single and
744 electrically coupled neurons in different animals. Nature neuroscience. 2006;9(3):356.

745 34. Taylor AL, Goaillard J-M, Marder E. How multiple conductances determine
746 electrophysiological properties in a multicompartment model. Journal of Neuroscience.
747 2009;29(17):5573–5586.

748 35. O'Leary T, Williams AH, Caplan JS, Marder E. Correlations in ion channel expression emerge
749 from homeostatic tuning rules. Proceedings of the National Academy of Sciences.
750 2013;110(28):E2645–E2654.

751 36. Ranjan R, Khazen G, Gambazzi L, Ramaswamy S, Hill SL, Schürmann F, et al. Channelpedia: an
752 integrative and interactive database for ion channels. Frontiers in neuroinformatics.
753 2011;5:36.

754 37. Podlaski WF, Seeholzer A, Groschner LN, Miesenböck G, Ranjan R, Vogels TP. Mapping the
755 function of neuronal ion channels in model and experiment. Elife. 2017;6:e22152.

38. Wei H, Bonjean M, Petry HM, Sejnowski TJ, Bickford ME. Thalamic burst firing propensity: a comparison of the dorsal lateral geniculate and pulvinar nuclei in the tree shrew. Journal of Neuroscience. 2011;31(47):17287–17299.

39. Connelly WM, Crunelli V, Errington AC. Passive synaptic normalization and input synchrony-dependent amplification of cortical feedback in thalamocortical neuron dendrites. Journal of Neuroscience. 2016;36(13):3735–3754.

40. Tennøe S, Halnes G, Einevoll GT. Uncertainpy: A Python toolbox for uncertainty quantification and sensitivity analysis in computational neuroscience. bioRxiv. 2018;274779.

41. Markram H, Muller E, Ramaswamy S, Reimann MW, Abdellah M, Sanchez CA, et al. Reconstruction and simulation of neocortical microcircuitry. Cell. 2015;163(2):456–492.

42. BlueBrain. BlueBrain/eFEL [Internet]. 2018. Available from: https://github.com/BlueBrain/eFEL

43. RStudio Team. RStudio: Integrated Development Environment for R [Internet]. Boston, MA: RStudio, Inc.; 2016. Available from: http://www.rstudio.com/

44. Choisy M. Identifying a cutoff value from bimodal data [Internet]. 2018. Available from: http://marcchoisy.free.fr/fmm/index.html

45. BlueBrain. BlueBrain/NeuroM [Internet]. 2018. Available from: https://github.com/BlueBrain/NeuroM

774 46. O'Reilly C, Iavarone E, Hill SL. A Framework for Collaborative Curation of Neuroscientific
775 Literature. Frontiers in neuroinformatics. 2017;11:27.

776 47. Hille B. Ionic channels in excitable membranes. Current problems and biophysical
777 approaches. Biophysical Journal. 1978;22(2):283–294.

778 48. Parri HR, Crunelli V. Sodium current in rat and cat thalamocortical neurons: role of a non-
779 inactivating component in tonic and burst firing. Journal of Neuroscience. 1998;18(3):854–
780 867.

781 49. Budde T, Biella G, Munsch T, Pape H-C. Lack of Regulation by Intracellular Ca2+ of the Hyper
782 Polarization-Activated Cation Current in Rat Thalamic Neurones. The Journal of physiology.
783 1997;503(1):79–85.

784 50. McCormick D a, Huguenard JR. A model of the electrophysiological properties of
785 thalamocortical relay neurons. Journal of neurophysiology. 1992;68(4):1384–1400.

786 51. McCORMICK DA, Pape H-C. Properties of a hyperpolarization-activated cation current and its
787 role in rhythmic oscillation in thalamic relay neurones. The Journal of physiology.
788 1990;431(1):291–318.

789 52. Magistretti J, Alonso A. Biophysical properties and slow voltage-dependent inactivation of a
790 sustained sodium current in entorhinal cortex layer-II principal neurons: a whole-cell and
791 single-channel study. The Journal of general physiology. 1999;114(4):491–509.

792 53. Huguenard J, Coulter D, Prince D. A fast transient potassium current in thalamic relay
793 neurons: kinetics of activation and inactivation. Journal of neurophysiology.
794 1991;66(4):1304–1315.

795 54. Ehling P, Cerina M, Meuth P, Kanyshkova T, Bista P, Coulon P, et al. Ca2+-dependent large
796 conductance K+ currents in thalamocortical relay neurons of different rat strains. Pflügers
797 Archiv-European Journal of Physiology. 2013;465(4):469–480.

798 55. Gymnopoulos M, Cingolani LA, Pedarzani P, Stocker M. Developmental mapping of small-
799 conductance calcium-activated potassium channel expression in the rat nervous system.
800 Journal of Comparative Neurology. 2014;522(5):1072–1101.

801 56. Köhler M, Hirschberg B, Bond C, Kinzie JM, Marrion N, Maylie J, et al. Small-conductance,
802 calcium-activated potassium channels from mammalian brain. Science.
803 1996;273(5282):1709–1714.

804 57. Hines ML, Carnevale NT. The NEURON simulation environment. Neural computation.
805 1997;9(6):1179–1209.

806 58. McDougal RA, Morse TM, Carnevale T, Marenco L, Wang R, Migliore M, et al. Twenty years
807 of ModelDB and beyond: building essential modeling tools for the future of neuroscience. J
808 Comput Neurosci. 2017 Feb 1;42(1):1–10.

809 59. BlueBrain. BlueBrain/BluePyOpt [Internet]. 2018. Available from:
810 https://github.com/BlueBrain/BluePyOpt

811 60. Weaver CM, Wearne SL. Neuronal firing sensitivity to morphologic and active membrane
812 parameters. PLoS Computational Biology. 2008;4(1):e11.

813 61. Olifer AV. Neuronal Parameter Sensitivity. In: Jaeger D, Jung R, editors. Encyclopedia of
814 Computational Neuroscience [Internet]. New York, NY: Springer New York; 2013 [cited 2018
815 Dec 19]. p. 1–6. Available from: https://doi.org/10.1007/978-1-4614-7320-6_172-1

816